Active microrheology, Hall effect, and jamming in chiral fluids

C. Reichhardt and C. J. O. Reichhardt
Theoretical Division and Center for Nonlinear Studies, Los Alamos National Laboratory, Los Alamos, New Mexico 87545, USA

(Received 30 January 2019; revised manuscript received 1 May 2019; published 15 July 2019)

We examine the motion of a probe particle driven through a chiral fluid composed of circularly swimming disks. We find that the probe particle travels in both the longitudinal direction, parallel to the driving force, and in the transverse direction, perpendicular to the driving force, giving rise to a Hall angle. Under constant driving force, we show that the probe particle velocity in both the longitudinal and transverse directions exhibits nonmonotonic behavior as a function of the activity of the circle swimmers. The Hall angle is maximized when a resonance occurs between the frequency of the chiral disks and the motion of the probe particle. As the density of the chiral fluid increases, the Hall angle gradually decreases before reaching zero when the system enters a jammed state. We show that the onset of jamming depends on the chiral particle swimming frequency, with a fluid state appearing at low frequencies and a jammed solid occurring at high frequencies.

DOI: 10.1103/PhysRevE.100.012604

I. INTRODUCTION

A variety of systems can be described as assemblies of particles that exhibit chiral or circular motion [1,2], such as circularly moving colloids [3–6], biological circle swimmers [7], active spinners [8–12], circularly driven particles [13–17], and chiral robot swarms [18]. Other systems in which chiral or gyroscopic motion occurs include skyrmions in chiral magnets [19,20] and classical charged particles moving in a magnetic field [21]. Such chiral particle assemblies can exhibit a variety of dynamical phases such as large-scale rotations [18], self-assembly [5,6,8,9,11], edge currents [5,9,15,22], and odd-viscosity responses [10,23,24].

Damping, fluctuations, and jamming in particle assemblies can be examined at the local level using active rheology, which is based on the response of a probe particle that is driven at either constant force or constant velocity through a fluid or jammed medium [25–30]. Active rheology has been applied to the onset of jamming [26,27,31–34], where the threshold for probe particle motion increases from zero to a finite value at the jamming transition. It has been used to measure changes in viscosity and diffusive responses [26,35–40] as well as velocity-force relations [25,26,32,41–44]. Active rheology has been applied not only to soft-matter systems, but also to the dynamics of individual vortices dragged across pinning landscapes in type-II superconductors [45–47]. In systems that are active rather than passive, active rheology shows large changes in the velocity of the probe particle as a function of increasing bath activity when the system transitions from a fluid state to an actively phase-separated state [48]. In each case, when the probe particle is driven at constant force, it moves in the direction of drive and exhibits symmetric fluctuations in the transverse direction, with no transverse drift or Hall velocity.

Here we study the active rheology of a probe particle driven through a chiral fluid of circularly swimming disks. We find that for low and intermediate fluid densities, the probe particle exhibits a longitudinal velocity $\langle V_{\rm long}\rangle$ in the direction of drive as well as a finite transverse or Hall velocity $\langle V_{\rm trans}\rangle$, giving rise to a Hall effect with a Hall angle of $\theta_{\rm Hall} = \arctan(\langle V_{\rm trans}\rangle/\langle V_{\rm long}\rangle)$. We examine the evolution of the Hall angle as a function of applied driving force, temperature, and chiral fluid density, and find Hall angles that are as large as $\theta_{\rm Hall} = 45^\circ$. We also observe nonmonotonic behavior of $\theta_{\rm Hall}$ in which the transverse velocity is maximized when a commensuration occurs between the chiral disk rotation frequency and the time interval between consecutive collisions of the probe particle with the chiral disks. In general, $\theta_{\rm Hall}$ decreases with increasing chiral disk density, and it drops to zero at high densities when a jammed state appears. In the dense limit, the probe particle can move only when the driving force is larger than a finite threshold value, and this threshold depends strongly on the chiral disk swimming frequency. At low frequencies, the threshold is nearly zero, while at high frequencies, the threshold increases when the system acts like a solid. We compare the dynamics of the probe particle to driven skyrmions, which have recently been shown to exhibit a skyrmion Hall effect that also exhibits nonmonotonic behavior as a function of dc drive, temperature, and skyrmion density [49–53].

II. SIMULATION AND SYSTEM

We consider a two-dimensional $L \times L$ system with $L = 36$ in which we place N nonoverlapping disks with a radius $R_d = 0.5$, where the disks have repulsive harmonic interactions. The density of the system is characterized by the area covered by the disks, $\phi = N\pi R_d^2/L^2$. For monodisperse disks at $T = 0$, when $\phi = 0.9$ the system forms a triangular solid in which the disks are just touching. The force between disks i and j is given by $\mathbf{F}_{pp}^{ij} = k(r_{ij} - 2R_d)\Theta(r_{ij} - 2R_d)\hat{\mathbf{r}}_{ij}$, where $r_{ij} = |\mathbf{r}_i - \mathbf{r}_j|$, $\hat{\mathbf{r}}_{ij} = (\mathbf{r}_i - \mathbf{r}_j)/r_{ij}$, and Θ is the Heaviside step function. The spring stiffness is set to $k = 50$, ensuring that the maximum overlap between disks is less than one percent. The densities and parameters we consider here have also been studied in previous works [15,32,48]. The dynamics of disk

i is determined by the following overdamped equation of motion:

$$\eta \frac{d\mathbf{r}_i}{dt} = \sum_{j \neq i}^{N} \mathbf{F}_{pp}^{ij} + \mathbf{F}_{\rm circ}^{i} + \mathbf{F}_{i}^{T}. \quad (1)$$

We set the damping constant $\eta = 1$ and our simulation time step is $\Delta t = 0.002$. Here $\mathbf{F}_{\rm circ}^{i}$ is a driving force that creates a circular motion of the disks of the form $\mathbf{F}_{\rm circ}^{i} = A[\sin(\omega t)\hat{\mathbf{x}} + \cos(\omega t)\hat{\mathbf{y}}]$, controlled by varying the drive amplitude A. All of the chiral disks move in phase with each other. The thermal force F^T is produced by Langevin kicks with the properties $\langle F_i^T(t)\rangle = 0$ and $\langle F_i^T(t)F_j^T(t')\rangle = 2\eta k_B T\delta_{ij}\delta(t-t')$. Unless otherwise noted, we fix $F^T = 2.0$, a value large enough to maintain the system in a liquid state up to the solidification density $\phi = 0.9$. We note that the thermal kicks cause each particle to undergo diffusive behavior at long timescales, which could be appropriate for many types of active colloidal systems. To create our probe particle, we select a single disk and replace $\mathbf{F}_{\rm circ}^{i}$ with $\mathbf{F}_D = F_D\hat{\mathbf{x}}$. We measure the average velocity response in the longitudinal direction, $\langle V_{\rm long}\rangle = \sum_i^{T_a} \mathbf{v}_p(t_i)\cdot\hat{\mathbf{x}}$, as well as in the transverse direction, $\langle V_{\rm trans}\rangle = \sum_i^{T_a} \mathbf{v}_p(t_i)\cdot\hat{\mathbf{y}}$, where $\mathbf{v}_p(t_i)$ is the instantaneous velocity of the probe particle. These quantities are averaged over an interval of $T_a = 5\times10^6$ time steps, which is long enough to ensure that the system has reached a steady dynamical state for the parameters we consider. In the absence of collisions between the probe particle and the chiral disks, we obtain the free-flow value $\langle V_{\rm long}\rangle = F_D/\eta$.

We focus on two regimes. The first is well below the jamming density at $\phi = 0.424$ and $F^T = 2.0$, where the system forms a liquid state, and the second is in a high-density regime at $\phi = 0.8482$, close to the jamming limit, where the disks exhibit a finite depinning threshold below which motion does not occur. In the low-density regime, we consider a finite chiral activity with $A = 2.5$ and $\omega = 0.006$. Here the effects of the active rotation are maximized near $F_D = 1.0$ when the active disks undergo one rotation during the mean interval between collisions with the probe particle. We also study the passive $A = 0$ case with the same parameters. We examine the effects of varying A, ω, F_D, and F^T, as well as the variation of the density ϕ for fixed activity, and in all cases we show that the transverse response can be maximized at an optimum parameter value.

III. RESULTS

In Fig. 1 we show an image of the system highlighting the chiral disk locations and trajectories over a fixed period of time for a system with $\phi = 0.181$, $A = 2.5$, $\omega = 0.006$, and a thermal force of $F^T = 2.0$. The disks execute circular orbits, and the center of mass of each circular orbit has a diffusive behavior. The red disk is the probe particle, which does not experience a circular drive but instead moves under a force F_D applied in the x direction, as indicated by the arrow.

In Figs. 2(a) and 2(b) we plot $\langle V_{\rm long}\rangle$ and $\langle V_{\rm trans}\rangle$, respectively, versus F_D in a system with $\phi = 0.424$, $A = 2.5$, and $\omega = 0.006$. Here $\langle V_{\rm long}\rangle$ monotonically increases with increasing F_D and there is no threshold for motion, while $\langle V_{\rm trans}\rangle$

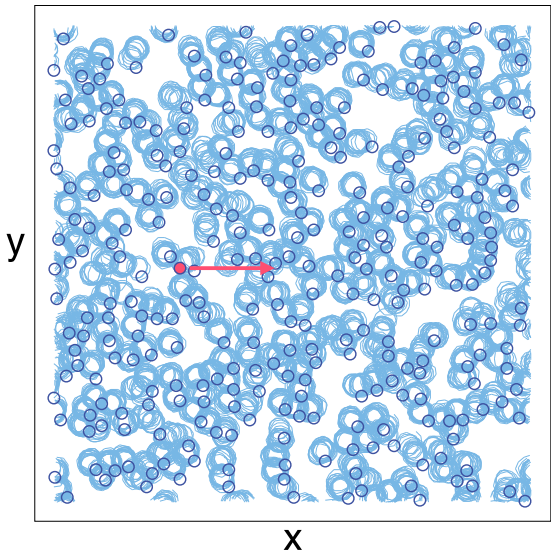

FIG. 1. Instantaneous positions (dark blue circles) and trajectories (light blue lines) of chiral disks during a fixed period of time along with the position (red circle) and driving direction (red arrow) of the probe particle in a sample with $\phi = 0.181$, $A = 2.5$, $\omega = 0.006$, $F^T = 2.0$, and $F_D = 2.0$. The chiral disks undergo a combination of diffusion and circular motion.

increases with increasing drive at low F_D before reaching a maximum near $F_D = 1.25$ and then decreasing again. Since both the longitudinal and transverse velocities are finite, the driven particle is moving at an angle with respect to drive direction, similar to the Hall effect found for the motion of a charged particle in a magnetic field. We plot the Hall angle $\theta_{\rm Hall} = \tan^{-1}(\langle V_{\rm trans}\rangle/\langle V_{\rm long}\rangle)$ versus F_D in Fig. 2(c). The maximum value of $\theta_{\rm Hall} = 23^\circ$ occurs at $F_D = 0.75$, a drive

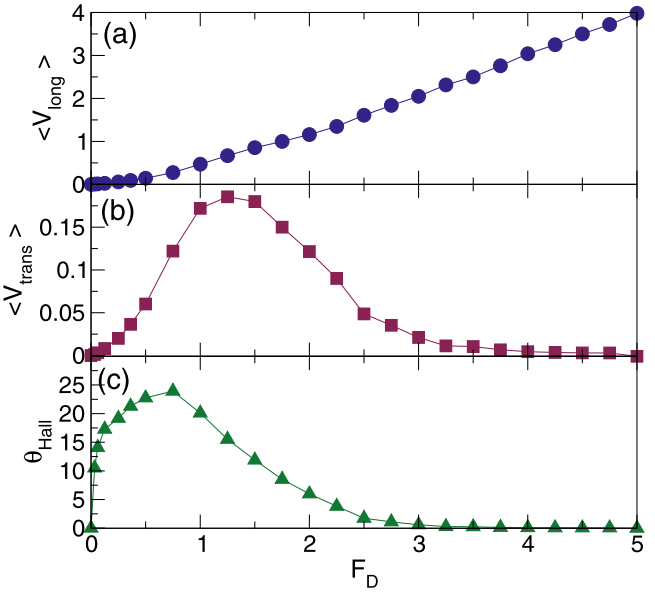

FIG. 2. Local probe response in a system with $\phi = 0.424$, $A = 2.5$, and $\omega = 0.006$. (a) The longitudinal velocity $\langle V_{\rm long}\rangle$ vs F_D. (b) The transverse velocity $\langle V_{\rm trans}\rangle$ vs F_D. (c) The Hall angle $\theta_{\rm Hall} = \tan^{-1}(\langle V_{\rm trans}\rangle/\langle V_{\rm long}\rangle)$ vs F_D.

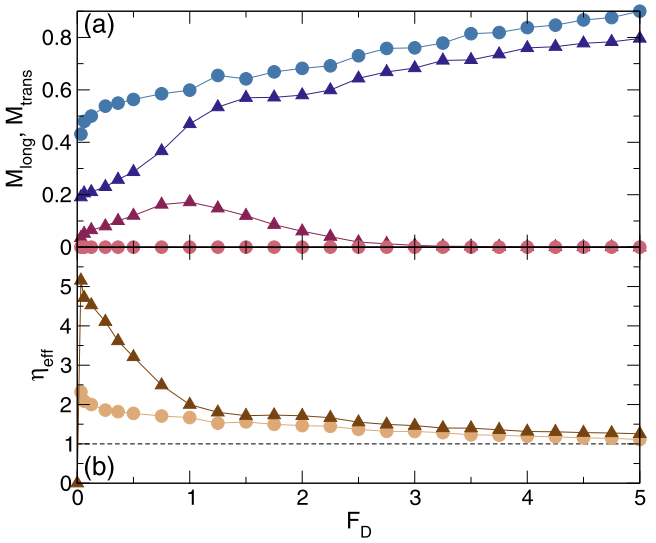

FIG. 3. (a) The longitudinal motility $M_{\rm long} = \langle V_{\rm long}\rangle/F_D$ vs F_D for the active system in Fig. 1 (dark blue triangles) and for a passive system with $A = 0$ (light blue circles). Also plotted is the transverse mobility $M_{\rm trans} = \langle V_{\rm trans}\rangle/F_D$ vs F_D for the same active (dark red triangles) and passive (light red circles) systems. (b) The effective damping $\eta_{\rm eff}$ obtained from the net velocity $\langle V\rangle = (\langle V_{\rm trans}\rangle^2 + \langle V_{\rm long}\rangle^2)^{1/2}$ for the active (dark brown triangles) and passive (light brown circles) systems. The damping is enhanced in the active system, particularly at low drives. The black dashed line indicates the damping $\eta = 1$ experienced by an isolated free particle.

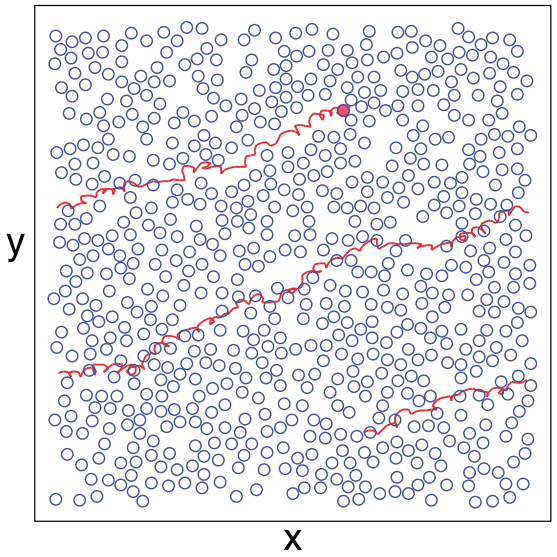

FIG. 4. Instantaneous positions of chiral disks (dark blue circles) and probe particle (red circle) along with the probe particle trajectory (red line) over a period of time for the system in Fig. 2 with $\phi = 0.424$, $A = 2.5$, and $\omega = 0.006$ at $F_D = 1.0$, where the probe particle moves at an average Hall angle of $\theta_{\rm Hall} = 20^\circ$.

smaller than the value of $F_D = 1.26$ at which the maximum in $\langle V_{\rm trans}\rangle$ appears. For higher drives, $\theta_{\rm Hall}$ gradually deceases, reaching a value close to zero for $F_D > 4.0$.

We measure the longitudinal mobility $M_{\rm long} = \langle V_{\rm long}\rangle/F_D$ and transverse mobility $M_{\rm trans} = \langle V_{\rm trans}\rangle/F_D$ for the system in Fig. 2 and show the resulting curves in Fig. 3(a). Starting from a small value, $M_{\rm long}$ increases with increasing F_D until it approaches the free-flow limit of $M_{\rm long} = 1$ at high drives. In contrast, $M_{\rm trans}$ increases to a maximum value of $M_{\rm trans} \approx 0.2$ near $F_D = 1.0$ and then decreases to $M_{\rm trans} = 0$ at high drives. For comparison, in Fig. 3(a) we also plot the behavior of $M_{\rm long}$ and $M_{\rm trans}$ in the $A = 0$ or inactive limit, where $M_{\rm trans} = 0$ for all values of F_D. The value of $M_{\rm long}$ is always higher in the inactive system than in the sample with finite chiral motion, indicating that the chiral motion increases the effective damping or viscosity experienced by the moving probe particle. A current topic in many chiral active matter systems is the question of odd-viscosity response [22–24], but it is not clear exactly what the signature of odd viscosity would be in the local driven probe system. In Fig. 3(b) we plot the effective damping constant $\eta_{\rm eff} = 1/\langle V\rangle$ versus F_D for the active and passive systems shown in Fig. 3(a). Here the net velocity is given by $\langle V\rangle = (\langle V_{\rm trans}\rangle^2 + \langle V_{\rm long}\rangle^2)^{1/2}$. The effective damping for $A = 0$ is largest at low F_D and decreases monotonically with increasing drive, gradually approaching the free-particle limit of $\eta = 1$ at high drives. When we introduce finite activity, we find a large increase in $\eta_{\rm eff}$ at low drives $F_D < 1$. This also means that the viscosity of the active system is larger, indicating that the active rotation increases the net damping in the system.

In Fig. 4 we illustrate the trajectory of the probe particle over a fixed time interval superimposed on a snapshot of the instantaneous chiral disk locations for the system in Fig. 2 at $F_D = 1.0$. The probe particle is moving at an angle of approximately $\theta_{\rm Hall} = 20^\circ$ with respect to the drive; however, there are local trajectory segments in which the Hall angle is larger or smaller than average.

The chiral disks have an intrinsic rotation frequency of ω, and therefore the time required for each chiral disk to complete one orbit is $\tau_P = 2\pi/\omega$. The average spacing between chiral disks is $a = 1/\sqrt{\phi}$. When the probe particle comes into contact with a chiral disk at small F_D, the chiral disk can complete multiple rotations during the time required for the probe particle to move out of interaction range since $F_D\tau_P \ll a$. As a result, the average transverse force exerted on the probe particle by the chiral disk is small and $\theta_{\rm Hall}$ is nearly zero. At high F_D, the probe particle is moving rapidly in the longitudinal direction and spends a very short time interacting with the chiral disks during a collision since $F_D\tau_P \gg a$, so once again the maximum transverse shift experienced by the probe particle is small and the Hall angle is small. Between these limits, a resonance can occur. When $\omega = 0.006$ and $\phi = 0.424$, as in Fig. 2, the average spacing between chiral disks is $a = 1.35$, and $\tau_P = 1047\Delta t$, where $\Delta t = 0.002$ is the size of a simulation time step. At $F_D = 0.75$, the probe particle would move a distance $F_D\tau_P = 1.57$ during one chiral rotation period in the absence of collisions with the chiral disks. Collisions reduce this travel distance to a value that is close to a, so that on average the probe particle interacts with a given chiral disk for one rotation period. This maximizes the chance that the chiral disk will exert a coordinated, monodirectional transverse force on the probe particle, resulting in a significant transverse displacement. The maximum in $\theta_{\rm Hall}$ thus arises due to a resonance between the chiral rotation timescale and

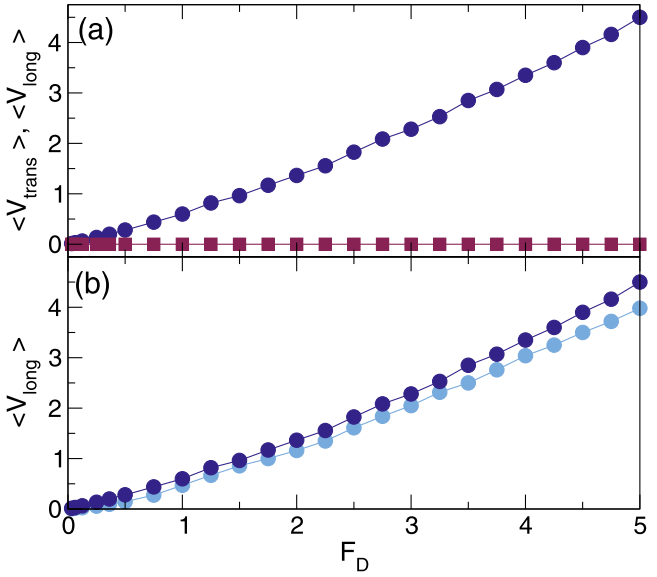

FIG. 5. (a) $\langle V_{\rm long}\rangle$ (dark blue circles) and $\langle V_{\rm trans}\rangle$ (red squares) vs F_D for a nonchiral fluid with the same parameters as in Fig. 2 except with $A = 0$. Here $\langle V_{\rm trans}\rangle = 0$ for all values of F_D. (b) $\langle V_{\rm long}\rangle$ (dark blue circles) vs F_D for the system in panel (a) at $A = 0.0$ and $\langle V_{\rm long}\rangle$ (light blue circles) vs F_D for the chiral system in Fig. 2 with $A = 2.5$, showing that the damping of the longitudinal motion is larger in the chiral fluid.

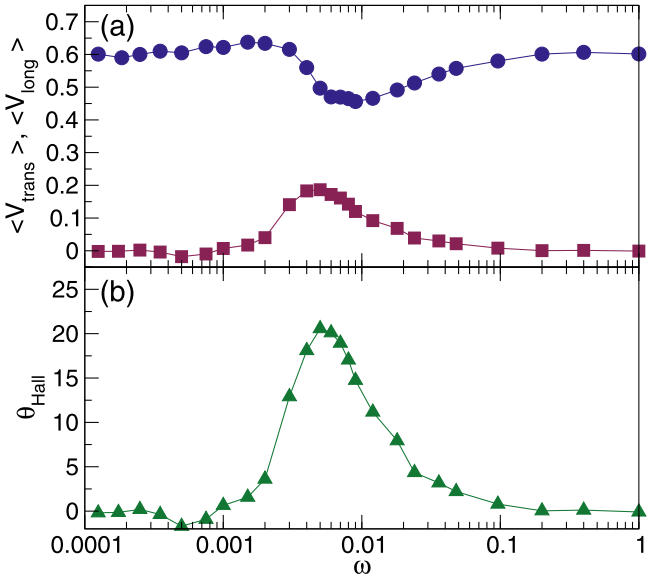

FIG. 6. (a) $\langle V_{\rm trans}\rangle$ (red squares) and $\langle V_{\rm long}\rangle$ (blue circles) vs ω for a system with $F_D = 1.0$, $A = 2.5$, and $\phi = 0.424$. A minimum in $\langle V_{\rm long}\rangle$ coincides with a maximum in $\langle V_{\rm trans}\rangle$ near $\omega = 0.008$. (b) The corresponding $\theta_{\rm Hall}$ vs ω showing a maximum Hall angle of $\theta_{\rm Hall} = 23^\circ$ near $\omega = 0.004$.

the collision timescale. For higher ω at the same chiral disk density ϕ, the peak in $\theta_{\rm Hall}$ shifts to higher values of F_D. We can compare these results to the behavior of $\theta_{\rm Hall}$ for driven skyrmions [49,51,52]. In the absence of pinning, $\theta_{\rm Hall}$ for the skyrmion system has a constant value determined by the materials properties [49]. When pinning is present, $\theta_{\rm Hall}$ gradually increases from zero at small F_D, similarly to what appears in Fig. 2(b). In the skyrmion case, $\theta_{\rm Hall}$ saturates to the intrinsic value at large F_D, while for the chiral liquid, $\theta_{\rm Hall}$ decreases as F_D increases above the peak value.

In Fig. 5(a) we plot $\langle V_{\rm long}\rangle$ and $\langle V_{\rm trans}\rangle$ versus F_D for a nonchiral fluid with the same parameters as in Fig. 2 but with $A = 0$. Here, $\langle V_{\rm long}\rangle$ increases monotonically with increasing F_D, similarly to the chiral system; however, $\langle V_{\rm trans}\rangle = 0$ for all values of F_D, indicating that $\theta_{\rm Hall} = 0$ and that it is the chiral motion of the bath particles that produces the Hall effect. We find that $\langle V_{\rm long}\rangle$ is slightly lower in the chiral liquid than for the $A = 0$ passive disks, as shown in Fig. 5(b), where we compare the $\langle V_{\rm long}\rangle$ versus F_D curves for the $A = 0$ system from Fig. 5(a) and the $A = 2.5$ system from Fig. 2(a). The $A = 2.5$ curve is lower for all F_D, indicating that the chirality of the bath particles increases the longitudinal drag on the probe particle.

In Fig. 6(a) we plot $\langle V_{\rm long}\rangle$ and $\langle V_{\rm trans}\rangle$ versus ω for a system with $\phi = 0.424$, $A = 2.5$, and $F_D = 1.0$. Here there is a dip in $\langle V_{\rm long}\rangle$ near $\omega = 0.008$ that coincides with a peak in $\langle V_{\rm trans}\rangle$. The corresponding $\theta_{\rm Hall}$ versus ω appears in Fig. 6(b), where the Hall angle reaches a maximum value of $\theta_{\rm Hall} = 23^\circ$ near $\omega = 0.004$. At low frequencies, the chiral disks are rotating so slowly that the response is close to that of a passive fluid, while at high frequencies, the chiral orbits diminish in radius and the system again behaves like a passive fluid.

Figure 7 shows $\theta_{\rm Hall}$ versus ω for the system in Fig. 6 at F_D values ranging from 0.125 to 4.0. The peak in $\theta_{\rm Hall}$ shifts to higher values of ω with increasing F_D since the chiral particles must rotate faster in order to meet the resonance condition $F_D\tau_P \sim a$ as F_D increases. The maximum value of $\theta_{\rm Hall}$ increases with decreasing F_D since the lower longitudinal velocity of the probe particle at the peak in $\theta_{\rm Hall}$ produces a longer collision time and thus a greater transfer of momentum from the chiral disks to the probe particle. The maximum Hall angle we observe at very low F_D is close to $\theta_{\rm Hall} = 45^\circ$.

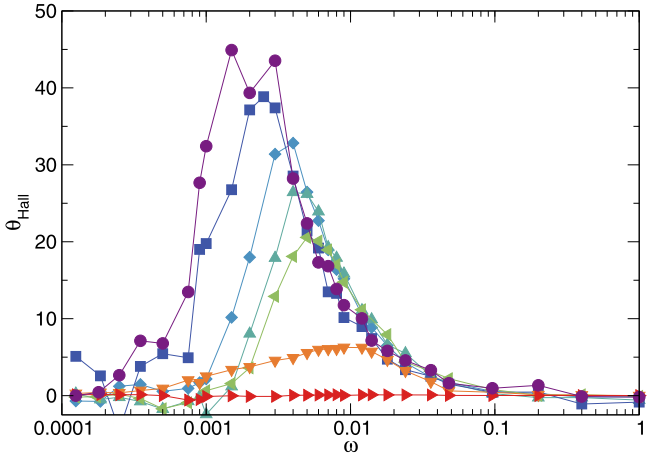

FIG. 7. $\theta_{\rm Hall}$ vs ω for the system in Fig. 6 with $A = 2.5$ and $\phi = 0.424$ for $F_D = 0.125$ (violet circles), 0.25 (dark blue squares), 0.5 (light blue diamonds), 0.75 (teal up triangles), 1.0 (green left triangles), 2.0 (orange down triangles), and 4.0 (red right triangles). Here the maximum in $\theta_{\rm Hall}$ shifts to higher ω with increasing F_D while the maximum possible Hall angle decreases.

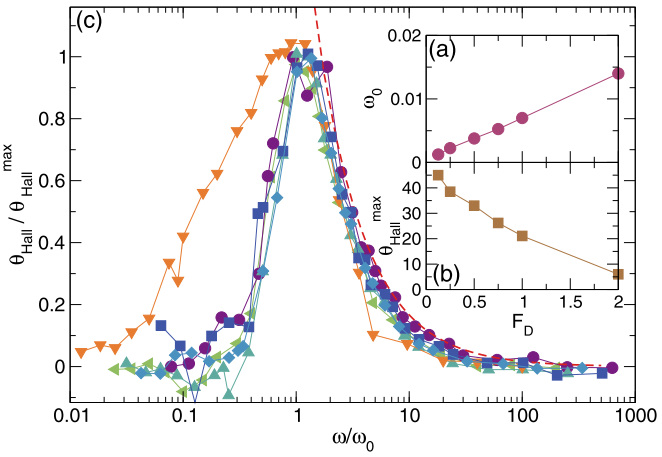

FIG. 8. (a) ω_0, the frequency at which the maximum Hall angle appears, vs F_D for the system in Fig. 7 with $A = 2.5$ and $\phi = 0.424$. There is a roughly linear increase in ω_0 with increasing F_D. (b) $\theta_{\rm Hall}^{\rm max}$, the value of the Hall angle at ω_0, vs F_D for the same system, showing a roughly linear decrease with F_D. (c) $\theta_{\rm Hall}/\theta_{\rm Hall}^{\rm max}$ vs ω/ω_0, showing a collapse of the curves in Fig. 7 based on the fits in panels (a) and (b). Here, $F_D = 0.125$ (violet circles), 0.25 (dark blue squares), 0.5 (light blue diamonds), 0.75 (teal up triangles), 1.0 (green left triangles), 2.0 (orange down triangles), and 4.0 (red right triangles). The thick dashed line is a fit to $\theta_{\rm Hall}/\theta_{\rm Hall}^{\rm max} \propto 1/\omega^*$ for $\omega^* > 0$, where $\omega^* \equiv \omega/\omega_0 - 1$.

In Fig. 8(a) we plot the frequency ω_0 at which $\theta_{\rm Hall}$ reaches its maximum value versus F_D for the system in Fig. 7. We find that ω_0 increases linearly with increasing F_D since it appears at a frequency for which a resonance occurs between the time required for an active disk to complete a revolution and the time that separates consecutive collisions between the probe particle and the active disks. The collision time is proportional to the probe velocity, which varies linearly with F_D, and therefore the resonant frequency ω_0 also varies linearly with F_D. We note that at lower F_D, where the probe velocity dependence on F_D becomes nonlinear, this behavior breaks down. In Fig. 8(b) we plot $\theta_{\rm Hall}^{\rm max}$, the maximum value of the Hall angle, versus F_D. Here $\theta_{\rm Hall}^{\rm max}$ decreases roughly linearly with increasing F_D, with some deviation from linearity at low values of F_D. Using the linear fits of ω_0 and $\theta_{\rm Hall}^{\rm max}$, we can collapse the curves from Fig. 7, as shown in the plot of $\theta_{\rm Hall}/\theta_{\rm Hall}^{\rm max}$ versus ω/ω_0 in Fig. 8(c). The dashed line in Fig. 8(c) is a fit to the form $\theta_{\rm Hall}/\theta_{\rm Hall}^{\rm max} \propto 1/\omega^*$ for $\omega^* > 0$, where $\omega^* \equiv \omega/\omega_0 - 1$, showing that $\theta_{\rm Hall}$ decays as an inverse power law above the resonant frequency.

In Fig. 9(a) we plot the trajectory of the probe particle and the positions of the chiral bath particles for the system in Fig. 7 at $F_D = 0.25$ and $\omega = 0.003$, where $\theta_{\rm Hall} \approx 45^\circ$. During some time intervals, the probe particle moves at an angle of nearly 90° with respect to the driving direction. Figure 9(b) illustrates the same sample at $F_D = 2.0$ and $\omega = 0.012$, where the Hall angle is much smaller, $\theta_{\rm Hall} = 6.5^\circ$.

In Fig. 10(a) we show $\langle V_{\rm trans}\rangle$ and $\langle V_{\rm long}\rangle$ versus A for a system with $\omega = 0.006$, $F_D = 1.0$, and $\phi = 0.424$. Here $\langle V_{\rm long}\rangle$ is large in the $A = 0$ passive limit, and it decreases with increasing A, passing through a local minimum near $A = 7.0$. We find that there is a threshold value $A_c = 0.5$

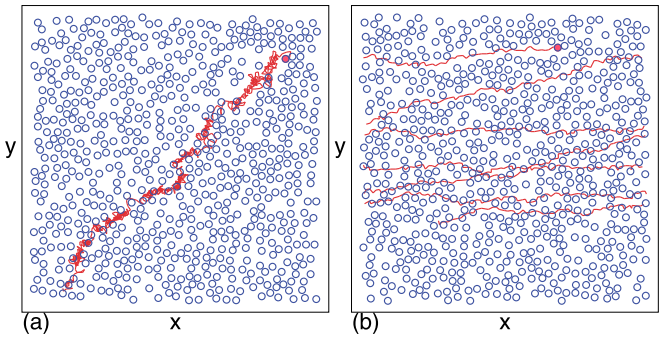

FIG. 9. Instantaneous positions of chiral disks (dark blue circles) and probe particle (red circle) along with the probe particle trajectory (red line) over a period of time for the system in Fig. 7 with $A = 2.5$ and $\phi = 0.424$. (a) $F_D = 0.25$ and $\omega = 0.003$, where $\theta_{\rm Hall} \approx 45^\circ$. (b) $F_D = 2.0$ and $\omega = 0.012$, where $\theta_{\rm Hall} = 6.5^\circ$.

below which $\langle V_{\rm trans}\rangle = 0$ and there is no transverse response, while a local maximum in $\langle V_{\rm trans}\rangle$ appears at $A = 4.0$. We plot the corresponding $\theta_{\rm Hall}$ versus A in Fig. 10(b), where the maximum value of $\theta_{\rm Hall} = 27^\circ$ occurs near $A = 4.0$.

In Fig. 11(a) we plot $\langle V_{\rm long}\rangle$ and $\langle V_{\rm trans}\rangle$ versus ϕ for a system with $A = 2.5$, $F_D = 1.0$, and $\omega = 0.006$, while in Fig. 11(b) we plot the corresponding $\theta_{\rm Hall}$ versus ϕ. At the lowest densities, the probe particle undergoes few collisions and moves in the free-flow limit with $\langle V_{\rm long}\rangle/F_D = 1.0$ and $\langle V_{\rm trans}\rangle = 0$. As ϕ increases, the probe particle velocity gradually decreases, dropping to zero near $\phi = 0.86$, which is the effective jamming density for these parameters. The decrease in the mobility of the probe particle with increasing density and the vanishing of the mobility as a jamming or crystallization density is approached resembles what was found in previous studies of active rheology for nonchiral passive disk

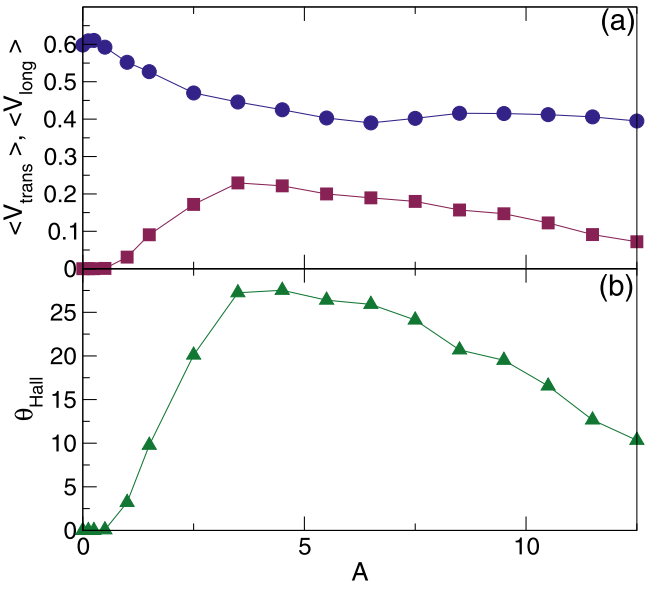

FIG. 10. (a) $\langle V_{\rm long}\rangle$ (blue circles) and $\langle V_{\rm trans}\rangle$ (red squares) vs A for a system with $\omega = 0.006$, $F_D = 1.0$, and $\phi = 0.424$. (b) The corresponding $\theta_{\rm Hall}$ vs A. There is a threshold value of $A_c = 0.5$ below which $\theta_{\rm Hall} = 0$ and the Hall response is absent.

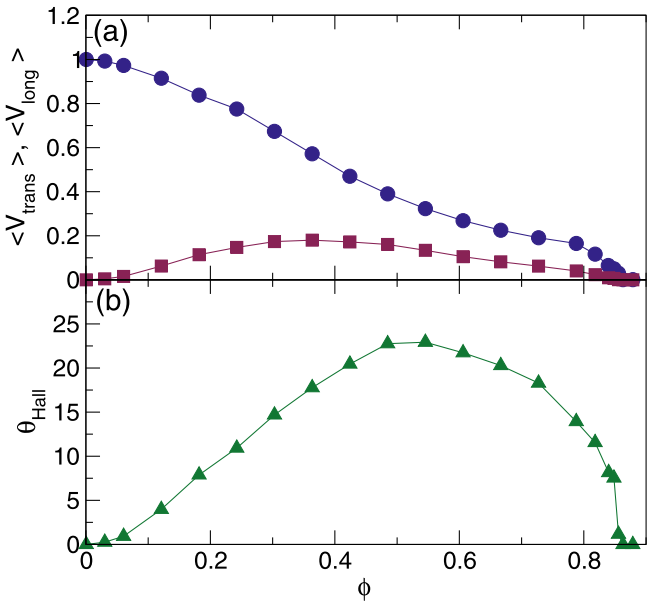

FIG. 11. (a) $\langle V_{\rm long}\rangle$ (blue circles) and $\langle V_{\rm trans}\rangle$ (red squares) vs ϕ for a system with $\omega = 0.006$, $F_D = 1.0$, and $A = 2.5$. (b) The corresponding $\theta_{\rm Hall}$ vs ϕ. A jamming transition occurs near $\phi = 0.86$.

systems [26,27,31,32]. In those studies, $\langle V_{\rm trans}\rangle = 0$ for all values of ϕ; however, for the chiral disks we find an increase in $\langle V_{\rm trans}\rangle$ with increasing density at low values of ϕ, with a maximum in $\langle V_{\rm trans}\rangle$ appearing near $\phi = 0.35$. This low-density increase in the transverse response results from the increasing frequency of collisions between the probe particle and the chiral disks, since it is these collisions that are responsible for the transverse probe particle motion. For $\phi > 0.35$, $\langle V_{\rm trans}\rangle$ decreases with increasing density due to a crowding effect, and at jamming $\langle V_{\rm trans}\rangle$ drops to zero. The maximum value of $\theta_{\rm Hall}$ occurs at a higher density of $\phi = 0.55$.

We note that in principle it would be possible to perform a collapse of $\langle V_{\rm trans}\rangle$, $\langle V_{\rm long}\rangle$, and $\theta_{\rm Hall}$ for varied values of ω, F_D, and A, similarly to what is shown in Fig. 8. The number of independent variables can be reduced slightly since the behavior as a function of A should be proportional to the behavior as a function of $1/\omega_p$, where $\omega_p \propto 1/(F_D + F_D^c)$ above the resonance and $\omega_p \propto 1/(F_D - F_D^c)$ below the resonance. Here F_D^c is the value of the dc drive at which the resonance occurs. Although we find that the drift velocity generally increases with F_D, we do not observe unbounded acceleration of the probe particle of the type that can occur in a Fermi acceleration process. This is expected since the inclusion of even a small amount of dissipation can destroy the Fermi acceleration mechanism [54].

We next consider the effect of changing the magnitude of the thermal fluctuations. In Fig. 12(a) we plot $\langle V_{\rm long}\rangle$ and $\langle V_{\rm trans}\rangle$ versus F^T for a system with $F_D = 1.0$, $\omega = 0.006$, $A = 2.5$, and $\phi = 0.424$. At $F^T = 0$, when the system is in the granular limit, the probe particle leaves a low-density wake behind it and $\langle V_{\rm trans}\rangle$ remains finite, indicating that thermal fluctuations are not necessary to produce the Hall response. In Fig. 12(a), $\langle V_{\rm trans}\rangle$ monotonically decreases with increasing F^T; however, there is a local minimum in $\langle V_{\rm long}\rangle$ near $F^T = 2.0$. The local minimum roughly coincides with the

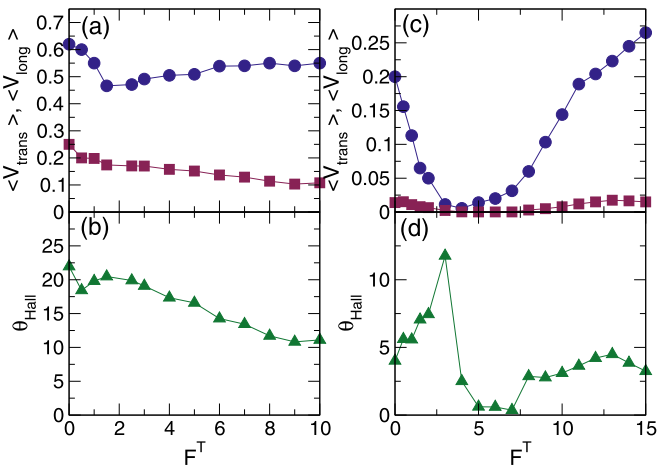

FIG. 12. (a) $\langle V_{\rm long}\rangle$ (blue circles) and $\langle V_{\rm trans}\rangle$ (red squares) vs F^T for a system with $\omega = 0.006$, $F_D = 1.0$, $A = 2.5$, and $\phi = 0.424$. (b) The corresponding $\theta_{\rm Hall}$ vs F_T. (c) $\langle V_{\rm long}\rangle$ (blue circles) and $\langle V_{\rm trans}\rangle$ (red squares) vs F^T for a system with $\omega = 0.006$, $F_D = 1.0$, $A = 2.5$, and $\phi = 0.8482$. (d) The corresponding $\theta_{\rm Hall}$ vs F_T. Here we find a freezing by heating phenomenon in the interval $4.0 < F^T < 7.0$.

crossover between low temperatures, where the probe leaves behind a low-density wake, and higher temperatures, where the wake rapidly refills with chiral disks. Figure 12(b) shows that the corresponding $\theta_{\rm Hall}$ versus F^T has its maximum value at $F^T = 0$, with a smaller local maximum appearing near $F^T = 2.0$. Above $F^T = 2.0$, $\theta_{\rm Hall}$ decreases monotonically with increasing F^T.

In Fig. 13(a) we illustrate the probe particle motion for the system in Fig. 12(a) with $\phi = 0.424$ at $F^T = 0$, where the probe particle moves at a finite Hall angle and leaves a low-density wake in its path. The appearance of an empty region behind the probe particle is similar to what has been observed for active rheology of nonthermal granular materials below the jamming density [27,32,33], since in these systems there is no energy penalty for the formation of a void.

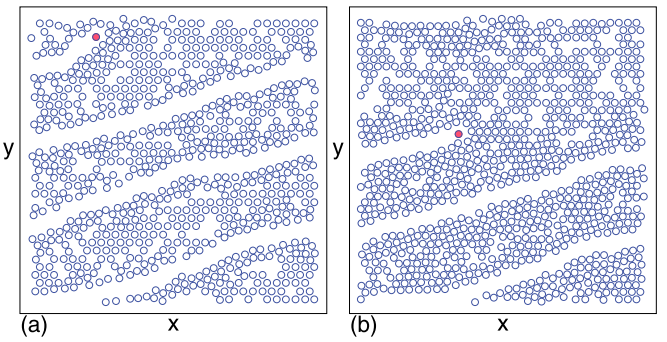

FIG. 13. Instantaneous positions of chiral disks (dark blue circles) and probe particle (red circle) for the system in Fig. 12(a) with $\omega = 0.006$, $F_D = 1.0$, $A = 2.5$, and $\phi = 0.424$ at $F^T = 0$, where the probe particle has a finite Hall angle but leaves a low-density depletion zone or wake behind as it moves. (b) The same system at a higher density of $\phi = 0.67$. Here the probe particle mobility is reduced but the Hall angle remains finite and the depletion zone persists.

At finite F^T, the chiral disks diffusively fill-in the empty space. In Fig. 13(b) we show the probe particle motion over the same time interval in a denser system with $F^T = 0$ and $\phi = 0.67$. The probe particle does not translate as far due to the decrease in mobility; however, it still leaves behind a low-density wake.

In Fig. 12(c) we plot $\langle V_{\rm long}\rangle$ and $\langle V_{\rm trans}\rangle$ versus F^T for a high-density system with $\phi = 0.8482$, $\omega = 0.006$, $A = 2.5$, and $F_D = 1.0$, and in Fig. 12(d) we show the corresponding $\theta_{\rm Hall}$ versus F^T. These parameters fall within a low-mobility regime, where the probe particle is not stuck but can only move relatively slowly through the chiral bath. At $F^T = 0$, $\langle V_{\rm long}\rangle \approx 0.2$ and $\theta_{\rm Hall} = 4.5^\circ$. As F^T increases, both $\langle V_{\rm long}\rangle$ and $\langle V_{\rm trans}\rangle$ decrease, reaching a value that is close to zero near $F^T = 4.0$. This is a signature of a thermally induced jamming transition that occurs when the thermal fluctuations increase the effective size of the bath particles and raise the effective density of the system to the jamming density. Such a transition can also be regarded as an example of a freezing by heating phenomenon in which the thermal fluctuations can effectively freeze the disks into a jammed state [55]. If the thermal fluctuations are finite but small, the chiral disks maintain their ordering in the jammed state and the probe particle slowly makes its way through the resulting mostly triangular solid. As F^T increases, the fluctuations become strong enough to melt the chiral disk crystal. As a result, liquid behavior reappears and the probe particle mobility rebounds, leading to the increase in both $\langle V_{\rm long}\rangle$ and $\langle V_{\rm trans}\rangle$ for $F^T > 6.0$. The Hall angle $\theta_{\rm Hall}$ in Fig. 12(d) passes through a local maximum near $F^T = 2.5$ just before the onset of thermally induced jamming, and it drops nearly to zero within the jammed state when the probe particle motion becomes extremely slow. For $F^T > 6.5$, when the jammed state melts and the probe particle mobility increases, $\theta_{\rm Hall}$ increases back to its prejammed level. These results indicate that a finite Hall effect can be observed even in nonthermal chiral systems.

Near the jammed state at high chiral disk densities, the behavior of $\theta_{\rm Hall}$ depends strongly on F_D and ω, since the probe particle can only move through the jammed chiral disks if the driving force is larger than a depinning threshold F_c. A monodisperse assembly of passive disks at $T = 0$ forms a triangular solid at a density of $\phi = 0.9$. For densities close to but below this solidification density, the addition of thermal fluctuations can induce freezing by heating or the formation of grain boundaries and other defects, and the disks exhibit glassy or very slow dynamics for densities in the range $0.83 < \phi < 0.9$. In our chiral disk system at $F^T = 2.0$ and $\phi = 0.8482$, the probe particle is mobile when $F_D = 1.0$, but if we reduce F_D we find that there is a finite threshold drive F_c below which the probe particle is no longer able to move. This is illustrated in Fig. 14(a), where we plot $\langle V_{\rm long}\rangle$ and $\langle V_{\rm trans}\rangle$ versus F_D for a system with $\phi = 0.8482$, $\omega = 0.006$, $F^T = 2.0$, and $A = 2.5$. Here $\langle V_{\rm long}\rangle = \langle V_{\rm trans}\rangle = 0$ when $F_D < F_c$, where the threshold force $F_c = 0.6$. In the corresponding $\theta_{\rm Hall}$ versus F_D curve shown in Fig. 14(b), we find that $\theta_{\rm Hall} = 0$ for $F_D < 0.8$, indicating that within the window $F_c < F_D < 0.8$, the probe particle has a finite longitudinal velocity but exhibits no Hall effect. The Hall angle reaches its maximum value of $\theta_{\rm Hall} \approx 8.5$ near $F_D = 1.75$, and gradually decreases toward zero for higher drives. Since this system is at a finite

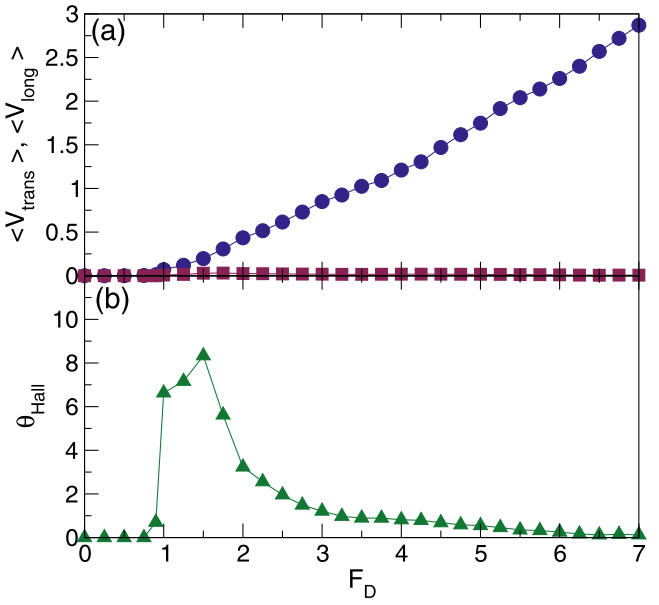

FIG. 14. (a) $\langle V_{\rm long}\rangle$ (blue circles) and $\langle V_{\rm trans}\rangle$ (red squares) vs F_D for a system with $\phi = 0.848$, $A = 2.5$, and $F^T = 2.0$. There is a finite depinning threshold near $F_D = 0.6$. (b) The corresponding $\theta_{\rm Hall}$ vs F_D passes through a maximum at $F_D = 1.75$.

temperature of $F^T = 2.0$, the probe particle is best described as undergoing a creep behavior at $F_D = 0.8$. During long periods of time, the probe particle is pinned, but there are occasional events in which the probe particle jumps to a new pinned location. Recent studies of driven skyrmions [51,56] showed that the Hall angle is zero in the creep regime and becomes finite at higher drives when the skyrmions transition to continuous flow, similarly to what we observe in Fig. 14; however, in the skyrmion case, $\theta_{\rm Hall}$ saturates to the intrinsic value at high drives rather than decreasing back to zero as in Fig. 14.

At high densities, we find that the threshold force F_c depends on the frequency at which the chiral disks rotate. In Fig. 15(a) we plot $\langle V_{\rm long}\rangle$ versus F_D in a system with $A = 2.5$, $F^T = 2.0$, and $\phi = 0.8482$ at $\omega = 0.008$, 0.006, 0.003, and 0.001. The threshold for motion is finite at $\omega = 0.006$ and $\omega = 0.008$, and zero for $\omega = 0.003$ and $\omega = 0.001$. In

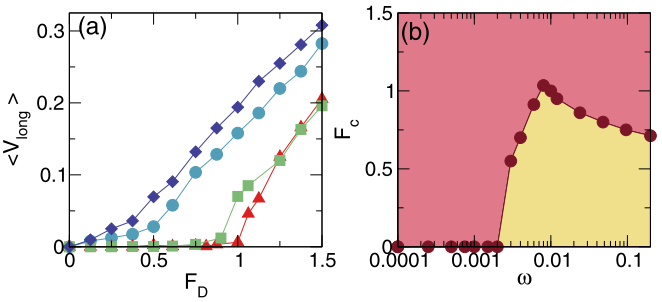

FIG. 15. (a) $\langle V_{\rm long}\rangle$ vs F_D for a system with $\phi = 0.8482$, $A = 2.5$, and $F^T = 2.0$ at $\omega = 0.008$ (red triangles), 0.006 (green squares), 0.003 (light blue circles), and 0.001 (dark blue diamonds). (b) The depinning force F_c vs ω for the same system highlighting regions in which the probe particle is moving (pink) or pinned (yellow).

Fig. 15(b) we show F_c versus ω for the system from Fig. 15(a). For drives above F_c, the probe can flow through the sample, but for drives below F_c, the probe particle is pinned. Here we find that F_c is finite only when $\omega > 0.003$, and that there is a local maximum in F_c near $\omega = 0.01$. We note that the appearance of a finite depinning threshold for a probe particle has been observed experimentally for systems in a high-density or glassy regime [26,57]. For the passive $A = 0$ limit in our system, we are always below the nonactive jamming density of 0.9, so the inclusion of activity can be viewed as effectively increasing the density of the particles. An open question is what effect the chiral activity would have on a system that is above the passive jamming density. For example, addition of activity could increase or decrease the critical depinning force. Our results indicate that at higher disk densities, the activity level of the chiral disks can be used to control a transition from jammed to unjammed behavior.

IV. SUMMARY

We have numerically examined the motion of a probe particle driven through a chiral liquid composed of circularly moving disks. In the absence of chirality, the probe particle drifts only in the direction of drive so there is no Hall effect; however, when the bath particles are chiral, both the longitudinal and transverse velocities of the probe particle are finite. Since a portion of the probe particle motion is perpendicular to the drive direction, the probe particle exhibits a finite Hall angle similar to what is observed for a charged particle moving in a magnetic field or for driven skyrmion systems. We find that the Hall angle has a nonmonotonic dependence on the probe particle driving force and the amplitude and frequency of the chiral disk motion. At low drives, the probe particle can undergo multiple collisions with an individual chiral bath particle, reducing the Hall angle, while at high drives the collisions between the probe and chiral bath particles are very brief, which again reduces the magnitude of the Hall angle. An optimal Hall angle occurs when the time between collisions of the probe particle with consecutive chiral bath particles is roughly equal to the time required for a chiral bath particle to complete a single rotation. We find that the Hall angle can reach values as large as $\theta_{\rm Hall} = 45^\circ$ and that the Hall effect persists in the zero-temperature or granular limit. When the chiral disk activity is fixed, the Hall angle is maximized at an optimal chiral disk density, while the probe particle velocity in both the longitudinal and transverse directions drops to zero when the chiral disks reach the jamming density, which is dependent on the frequency of the chiral motion. At low frequencies, the depinning threshold is zero and the probe particle is able to move under all applied drives, while at higher frequencies there is a finite depinning threshold, and for drives below this threshold, the probe particle is pinned. We compare our results with those obtained for skyrmions moving over random disorder, where drive-dependent Hall angles that increase with increasing drive are observed. In the skyrmion case, the Hall angle saturates to the clean limit at high drives, whereas for the chiral liquid we consider here, the Hall angle decreases to zero at high drives. Our results could be tested by driving probe particles through active chiral colloidal spinners, chiral granular matter, or even chiral robot swarms. Additionally, these results could be relevant to other systems that mimic chiral active baths, such as driving a single skyrmion through an array of other skyrmions or driving a single particle through an array of optical or fluid vortices.

Note added. Recently, we became aware of the work of Kumar *et al.* [58] on the motion of spinning probe particles through granular matter, where they report the onset of a Magnus-like effect including a lift force.

ACKNOWLEDGMENTS

We gratefully acknowledge the support of the US Department of Energy through the LANL/LDRD program for this work. This work was supported by the US Department of Energy through the Los Alamos National Laboratory. Los Alamos National Laboratory is operated by Triad National Security, LLC, for the National Nuclear Security Administration of the US Department of Energy (Contract No. 892333218NCA000001).

[1] H. Löwen, Chirality in microswimmer motion: From circle swimmers to active turbulence, Eur. Phys. J.: Spec. Top. **225**, 2319 (2016).

[2] C. Bechinger, R. Di Leonardo, H. Löwen, C. Reichhardt, G. Volpe, and G. Volpe, Active Brownian particles in complex and crowded environments, Rev. Mod. Phys. **88**, 045006 (2016).

[3] P. Tierno, T. Johansen, and T. Fischer, Localized and Delocalized Motion of Colloidal Particles on a Magnetic Bubble Lattice, Phys. Rev. Lett. **99**, 038303 (2007).

[4] F. Kümmel, B. ten Hagen, R. Wittkowski, I. Buttinoni, R. Eichhorn, G. Volpe, H. Löwen, and C. Bechinger, Circular Motion of Asymmetric Self-Propelling Particles, Phys. Rev. Lett. **110**, 198302 (2013).

[5] M. Han, J. Yan, S. Granick, and E. Luijten, Effective temperature concept evaluated in an active colloid mixture, Proc. Natl. Acad. Sci. USA **114**, 7513 (2017).

[6] G. Kokot, S. Das, R. G. Winkler, G. Gompper, I. S. Aranson, and A. Snezhko, Active turbulence in a gas of self-assembled spinners, Proc. Natl. Acad. Sci. USA **114**, 12870 (2017).

[7] W. R. DiLuzio, L. Turner, M. Mayer, P. Garstecki, D. B. Weibel, H. C. Berg, and G. M. Whitesides, *Escherichia coli* swim on the right-hand side, Nature (London) **435**, 1271 (2005).

[8] H. P. Nguyen, D. Klotsa, M. Engel, and S. C. Glotzer, Emergent Collective Phenomena in a Mixture of Hard Shapes through Active Rotation, Phys. Rev. Lett. **112**, 075701 (2014).

[9] B. C. van Zuiden, J. Paulose, W. T. M. Irvine, D. Bartolo, and V. Vitelli, Spatiotemporal order and emergent edge currents in

active spinner materials, Proc. Natl. Acad. Sci. USA **113**, 12919 (2016).
[10] D. Banerjee, A. Souslov, A. G. Abanov, and V. Vitelli, Odd viscosity in chiral active fluids, Nat. Commun. **8**, 1573 (2017).
[11] A. Aubret, M. Youssef, S. Sacanna, and J. Palacci, Targeted assembly and synchronization of self-spinning microgears, Nat. Phys. **14**, 1114 (2018).
[12] K. Dasbiswas, K. K. Mandadapu, and S. Vaikuntanathan, Topological localization in out-of-equilibrium dissipative systems, Proc. Natl. Acad. Sci. USA **115**, E9031 (2018).
[13] B. Liebchen and D. Levis, Collective Behavior of Chiral Active Matter: Pattern Formation and Enhanced Flocking, Phys. Rev. Lett. **119**, 058002 (2017).
[14] B.-Q. Ai, Z.-G. Shao, and W.-R. Zhong, Mixing and demixing of binary mixtures of polar chiral active particles, Soft Matter **14**, 4388 (2018).
[15] C. Reichhardt and C. J. O. Reichhardt, Reversibility, pattern formation, and edge transport in active chiral and passive disk mixtures, J. Chem. Phys. **150**, 064905 (2019).
[16] S. I. Denisov, T. V. Lyutyy, V. V. Reva, and A. S. Yermolenko, Temperature effects on drift of suspended single-domain particles induced by the Magnus force, Phys. Rev. E **97**, 032608 (2018).
[17] A. Maitra and M. Lenz, Spontaneous rotation can stabilise ordered chiral active fluids, Nat. Commun. **10**, 920 (2019).
[18] C. Scholz, M. Engel, and T. Pöschel, Rotating robots move collectively and self-organize, Nat. Commun. **9**, 931 (2018).
[19] N. Nagaosa and Y. Tokura, Topological properties and dynamics of magnetic skyrmions, Nat. Nanotechnol. **8**, 899 (2013).
[20] U. Ritzmann, S. von Malottki, J.-V. Kim, S. Heinze, J. Sinova, and B. Dupe, Trochoidal motion and pair generation in skyrmion and antiskyrmion dynamics under spin-orbit torques, Nat. Electron. **1**, 451 (2018).
[21] H. Goldstein, C. P. Poole, and J. L. Safko, *Classical Mechanics*, 3rd ed. (Addison-Wesley, New York, 2002).
[22] V. Soni, E. Bililign, S. Magkiriadou, S. Sacanna, D. Bartolo, M. J. Shelley, and W. T. M. Irvine, The free surface of a colloidal chiral fluid: Waves and instabilities from odd stress and Hall viscosity, arXiv:1812.09990.
[23] S. Ganeshan and A. G. Abanov, Odd viscosity in two-dimensional incompressible fluids, Phys. Rev. Fluids **2**, 094101 (2017).
[24] A. Souslov, K. Dasbiswas, M. Fruchart, S. Vaikuntanathan, and V. Vitelli, Topological Waves in Fluids with Odd Viscosity, Phys. Rev. Lett. **122**, 128001 (2019).
[25] M. B. Hastings, C. J. Olson Reichhardt, and C. Reichhardt, Depinning by Fracture in a Glassy Background, Phys. Rev. Lett. **90**, 098302 (2003).
[26] P. Habdas, D. Schaar, A. C. Levitt, and E. R. Weeks, Forced motion of a probe particle near the colloidal glass transition, Europhys. Lett. **67**, 477 (2004).
[27] J. A. Drocco, M. B. Hastings, C. J. Olson Reichhardt, and C. Reichhardt, Multiscaling at Point J: Jamming is a Critical Phenomenon, Phys. Rev. Lett. **95**, 088001 (2005).
[28] T. M. Squires and J. F. Brady, A simple paradigm for active and nonlinear microrheology, Phys. Fluids **17**, 073101 (2005).
[29] L. G. Wilson and W. C. K. Poon, Small-world rheology: An introduction to probe-based active microrheology, Phys. Chem. Chem. Phys. **13**, 10617 (2011).
[30] R. N. Zia, Active and passive microrheology: Theory and simulation, Annu. Rev. Fluid Mech. **50**, 371 (2018).
[31] R. Candelier and O. Dauchot, Journey of an intruder through the fluidization and jamming transitions of a dense granular media, Phys. Rev. E **81**, 011304 (2010).
[32] C. J. Olson Reichhardt and C. Reichhardt, Fluctuations, jamming, and yielding for a driven probe particle in disordered disk assemblies, Phys. Rev. E **82**, 051306 (2010).
[33] E. Kolb, P. Cixous, N. Gaudouen, and T. Darnige, Rigid intruder inside a two-dimensional dense granular flow: Drag force and cavity formation, Phys. Rev. E **87**, 032207 (2013).
[34] Y. Takehara and K. Okumura, High-Velocity Drag Friction in Granular Media Near the Jamming Point, Phys. Rev. Lett. **112**, 148001 (2014).
[35] A. M. Puertas and T. Voigtmann, Microrheology of colloidal systems, J. Phys.: Condens. Matter **26**, 243101 (2014).
[36] A. Fiege, M. Grob, and A. Zippelius, Dynamics of an intruder in dense granular fluids, Granular Matter **14**, 247 (2012).
[37] I. Gazuz, A. M. Puertas, Th. Voigtmann, and M. Fuchs, Active and Nonlinear Microrheology in Dense Colloidal Suspensions, Phys. Rev. Lett. **102**, 248302 (2009).
[38] R. N. Zia and J. F. Brady, Single-particle motion in colloids: Force-induced diffusion, J. Fluid Mech. **658**, 188 (2010).
[39] D. Winter, J. Horbach, P. Virnau, and K. Binder, Active Nonlinear Microrheology in a Glass-Forming Yukawa Fluid, Phys. Rev. Lett. **108**, 028303 (2012).
[40] R. P. A. Dullens and C. Bechinger, Shear Thinning and Local Melting of Colloidal Crystals, Phys. Rev. Lett. **107**, 138301 (2011).
[41] C. Reichhardt and C. J. Olson Reichhardt, Local Melting and Drag for a Particle Driven through a Colloidal Crystal, Phys. Rev. Lett. **92**, 108301 (2004).
[42] C. Mejía-Monasterio and G. Oshanin, Bias- and bath-mediated pairing of particles driven through a quiescent medium, Soft Matter **7**, 993 (2011).
[43] O. Bénichou, P. Illien, C. Mejía-Monasterio, and G. Oshanin, A biased intruder in a dense quiescent medium: Looking beyond the force-velocity relation, J. Stat. Mech. (2013) P05008.
[44] P. Illien, O. Bénichou, G. Oshanin, A. Sarracino, and R. Voituriez, Nonequilibrium Fluctuations and Enhanced Diffusion of a Driven Particle in a Dense Environment, Phys. Rev. Lett. **120**, 200606 (2018).
[45] E. W. J. Straver, J. E. Hoffman, O. M. Auslaender, D. Rugar, and K. A. Moler, Controlled manipulation of individual vortices in a superconductor, Appl. Phys. Lett. **93**, 172514 (2008).
[46] O. M. Auslaender, L. Luan, E. W. J. Straver, J. E. Hoffman, N. C. Koshnick, E. Zeldov, D. A. Bonn, R. Liang, W. N. Hardy, and K. A. Moler, Mechanics of individual isolated vortices in a cuprate superconductor, Nat. Phys. **5**, 35 (2009).
[47] X. Ma, C. J. O. Reichhardt, and C. Reichhardt, Manipulation of individual superconducting vortices and stick-slip motion in periodic pinning arrays, Phys. Rev. B **97**, 214521 (2018).
[48] C. Reichhardt and C. J. Olson Reichhardt, Active microrheology in active matter systems: Mobility, intermittency, and avalanches, Phys. Rev. E **91**, 032313 (2015).
[49] C. Reichhardt, D. Ray, and C. J. Olson Reichhardt, Collective Transport Properties of Driven Skyrmions with Random Disorder, Phys. Rev. Lett. **114**, 217202 (2015).

[50] C. Reichhardt and C. J. O. Reichhardt, Noise fluctuations and drive dependence of the skyrmion Hall effect in disordered systems, New J. Phys. **18**, 095005 (2016).

[51] W. Jiang, X. Zhang, G. Yu, W. Zhang, X. Wang, M. B. Jungfleisch, J. E. Pearson, X. Cheng, O. Heinonen, K. L. Wang, Y. Zhou, A. Hoffmann, and S. G. E. te Velthuis, Direct observation of the skyrmion Hall effect, Nat. Phys. **13**, 162 (2017).

[52] K. Litzius, I. Lemesh, B. Krüger, P. Bassirian, L. Caretta, K. Richter, F. Büttner, K. Sato, O. A. Tretiakov, J. Förster, R. M. Reeve, M. Weigand, I. Bykova, H. Stoll, G. Schütz, G. S. D. Beach, and M. Kläui, Skyrmion Hall effect revealed by direct time-resolved x-ray microscopy, Nat. Phys. **13**, 170 (2017).

[53] S. Woo, K. M. Song, X. Zhang, Y. Zhou, M. Ezawa, X.-X. Liu, S. Finizio, J. Raabe, N. J. Lee, S.-I. Kim, S.-Y. Park, Y. Kim, J.-Y. Kim, D. Lee, O. Lee, J. W. Choi, B.-C. Min, H. C. Koo, and J. Chang, Current-driven dynamics and inhibition of the skyrmion Hall effect of ferrimagnetic skyrmions in GdFeCo films, Nat. Commun. **9**, 959 (2018).

[54] E. D. Leonel and L. A. Bunimovich, Suppressing Fermi Acceleration in a Driven Elliptical Billiard, Phys. Rev. Lett. **104**, 224101 (2010).

[55] D. Helbing, I. J. Farkas, and T. Vicsek, Freezing by Heating in a Driven Mesoscopic System, Phys. Rev. Lett. **84**, 1240 (2000).

[56] C. Reichhardt and C. J. O. Reichhardt, Thermal creep and the skyrmion Hall angle in driven skyrmion crystals, J. Phys.: Condens. Matter **31**, 07LT01 (2019).

[57] N. Senbil, M. Gruber, C. Zhang, M. Fuchs, and F. Scheffold, Observation of Strongly Heterogeneous Dynamics at the Depinning Transition in a Colloidal Glass, Phys. Rev. Lett. **122**, 108002 (2019).

[58] S. Kumar, M. Dhiman, and K. A. Reddy, Magnus effect in granular media, Phys. Rev. E **99**, 012902 (2019).